AN ADAPTIVELY REFINED LEAST-SQUARES FINITE ELEMENT METHOD FOR GENERALIZED NEWTONIAN FLUID FLOWS USING THE CARREAU MODEL *

HSUEH-CHEN LEE†

Abstract. We implemented an adaptively refined least-squares finite element approach for the Navier-Stokes equations that govern generalized Newtonian fluid flows using the Carreau model. To capture the flow region, we developed an adaptive mesh refinement approach based on the least-squares method. The generated refined grids agree well with the physical attributes of the flows. We also proved that the least-squares approximation converges to the linearized versions solutions of the Carreau model at the best possible rate. Model problems considered in the study are the flow past a planar channel and 4-to-1 contraction problems. We presented the numerical results of the model problems, revealing the efficiency of the proposed scheme, and investigated the physical parameter effects.

Key words. least-squares, Carreau model, adaptive mesh refinement, generalized Newtonian fluid.

AMS subject classifications. 65N30, 65N50, 76M10

1. Introduction. An important non-Newtonian fluid is the generalized Newtonian fluid that describes viscous effects in the form of a shear-rate dependent viscosity. This fluid has been applied in the petroleum industry, chemical engineering, the food industry, medical science, and bioengineering [1]. Numerical algorithms have recently been developed to simulate flow problems [2, 3, 4]. Despite considerable progress, certain unsolved difficulties such as corner singularity and the computational limitations arising from the presence of multiple variables require a compatibility condition on finite element spaces when the standard mixed method approach is used [4].

Compared to Galerkin methods, least-squares methods based on finite element formulations have been shown to offer several theoretical and computational advantages for use in solving boundary value problems that arise in fields such as in [5]. Least-squares is easy to implement because the algebraic system generated by the discretization is always symmetric and positive definite, and a single approximating space for all variables can be used for programming least-squares finite element methods [6]. The Navier−Stokes equations can be expressed in terms of the primary variables (e.g., velocities and pressure), secondary variables (velocity gradients, vorticity, stream function, and stresses), or a combination of the two [7, 8, 9, 10, 11, 12]. In [12], the researchers presented a new reformulation of the Navier−Stokes equations containing the gradient of velocities and pressure. Their results revealed an improvement in both convergence rate and mass conservation accuracy relative to the original vorticity formulation. Bolton and Thatcher [11] presented a least-squares method for the stress and stream formulations of the Navier−Stokes equations. They discovered mass loss with an unweighted functional but achieved mass conservation through the appropriate weight. Deang and Gunzburger [13] also studied mass conservation in least-squares formulations and showed better mass conservation than an unweighted formulations, but the conditioning number of the resultant coefficient matrix became high. In [14], Bose and Carey presented a least-squares method using p-type finite elements and mesh redistribution for domains with singularities for upper-convected Maxwell and Bingham fluids. They indicated that scaling original differential equations is important for least-squares minimization. Nonlinear weighted least-squares methods (NWLS), based on the velocity-stress-pressure formu-

*This work was supported in part by the National Science Council of Taiwan under contract no. 100-2115-M-160-001.

†General Education Center, Wenzao Ursuline University of Languages, Kaohsiung 807, Taiwan (87013@mail.wzu.edu.tw).

lation of the Stokes equations, have recently applied to the Newtonian, Carreau, Oldroyd-B, and Giesekus models for numerical experiments [15, 4, 16]. The results derived from using uniform meshes indicated that when linear approximations in all variables were employed, the least-squares solutions exhibited numerical convergence rates of $O(h^2)$ in the L^2-norm for all dependent variables (or nearly so for the viscoelastic case). However, mathematical analysis of the least-squares functional for the Carreau model was not provided in [4] and the inertial effects were neglected in these results. In [17], the researchers indicated that the inertial term in the momentum equation cannot be neglected even in the case of very low Reynolds numbers. The inertia effects on non-Newtonian fluid flows should be discussed in future studies.

Although using NWLS methods obtains promising results, a difficulty in solving real case flow problems is the computational limitation arising from the large number of unknowns. To reduce the size of the linearized system of equations and resolve the singularities arising from geometric discontinuities, adaptive grids aligned with high gradient regions are often necessary to produce efficient and accurate results. In [18], Berger and Jameson indicated that the complex geometrical regions where the solution requires finer grid resolution are finely zoned in the initial grid generation phase, and the location of the inaccurate regions changes with changes in flow parameters. Adaptive finite element methods are being used extensively as powerful tools for approximating solutions of partial differential equations in a variety of application fields [19, 20, 21]. In [19], Sterck et al. investigated the behavior of two efficiency-based grid refinement strategies which take both error reduction and work into account for adaptive finite element solution to partial differential equations (PDEs). They indicated that use of a graded grid for elements with a singularity leads to significant improvement. Cai and Westphal [20] presented an adaptive mixed least-squares finite element method for steady Oldroyd type viscoelastic fluids, and adaptive mesh refinement is based on a nonlinear least-squares functional. They proved least-squares functional ellipticity and error bounds for linearized viscoelastic fluids. In [21], Adler et al. proposed new adaptive local refinement strategies for first-order system least-squares finite elements in conjunction with algebraic multigrid methods in the context of nested iteration. The algorithms choose which elements to refine based on optimal computational efficiency, taking into account both error reduction and computational cost. In [22], adaptive least-squares finite element methods for viscoelastic flow problems were developed. The results indicated that graded meshes agree with the physical attributes of these models and smoothed triangulation improves convergence rates and errors. However, grid effects of nonuniform meshes were also reported in [22] for the NWLS method using lower-order basis functions.

Based on these studies, we developed an adaptively refined least-squares approximation to the Carreau model of generalized Newtonian fluid flows. To avoid grid effects with nonlinear weighting function and mass loss with unweighted least-squares functional when lower-order basis functions are used, a linear weighted least-squares method involving appropriate mass conservation weights was used for the method. We approach nonlinear PDEs by linearizing the equations and then applying a least-squares method to them. We also derived the coercivity and continuity estimates for the homogeneous least-squares functional, which involves the sum of the equation residuals measured in the L^2-norm. The analysis of error bounds for the linearized generalized Newtonian fluid using the least-squares method follows the concept introduced in [23] and [20]. To capture the flow region, unlike previous research that uses optimal grids generated by equidistributing a grading function throughout the domain [22] and the least-squares functional [20], we developed a new adaptive algorithm based on the mesh redistribution with numerical solutions of velocity gradient refinement for a least-squares functional. We applied the graded recovery method to improve the accuracy

of the gradient velocity variable [24] and to refine grid points. We employed the nonlinear least-squares functional which is a posteriori error estimates to adjust the weight of the divergence term. When we used continuous piecewise linear finite element spaces for all variables, properly adjusting the importance of the mass conservation and with adaptive mesh refinements, the least-squares solutions exhibit optimal L^2-norm error convergence in all dependent variables. We extended the implementation to simulate the 4-to-1 contraction problem considered in [15] and addressed the physical parameter effects. In [3], Zinani and Frey presented a Galerkin least-squares (GLS) method with an equal order linear interpolation function that adds stabilized formulations for the Carreau model. We presented a least-squares finite element approach to the Carreau model for generalized Newtonian fluids, which makes use of a grading function to adaptively refine the mesh. Our solution method, least-squares is simpler than GLS, in which a stabilizing least-squares form of the governing equation is added to the Galerkin form. We showed that the results of the adaptively refined LS approach are compatible to those of the reduced GLS method presented by Zinani and Frey in [3]. We also showed that properly refined grids on areas where physical features vary rapidly are necessary for obtaining the expected accuracy.

The rest of this paper is organized as follows. Section 2 introduces the governing equations. Section 3 presents the notation, preliminaries, and coercivity and continuity of the homogeneous least-squares functional. Section 4 provides the error estimates of the L^2 least-squares approximations and the nonlinear iteration. Section 5 presents the adaptive grid generation algorithm for flow problems. Section 6 provides numerical results for the flow past a planar channel and a 4-to-1 contraction problem, and section 7 offers concluding remarks.

2. Governing Equations. Consider the steady-state, incompressible Navier−Stokes problem in a two-dimensional, Ω, with boundary Γ,

$$\begin{aligned} \mathbf{u}\cdot\nabla\mathbf{u} - \nabla\cdot\boldsymbol{\tau} + \nabla p &= \widehat{\mathbf{f}} \ \text{ in } \Omega, \\ \boldsymbol{\tau} - \frac{2\eta\left(\dot{\gamma}(\mathbf{u})\right)\mathbf{D}(\mathbf{u})}{\eta_0 Re} &= \mathbf{0} \ \text{ in } \Omega, \\ \nabla\cdot\mathbf{u} &= 0 \ \text{ in } \Omega, \\ \mathbf{u} &= \mathbf{0} \ \text{ on } \Gamma, \end{aligned} \tag{2.1}$$

where $\mathbf{D}(\mathbf{u}) = 0.5(\nabla\mathbf{u} + \nabla\mathbf{u}^T)$ is the standard strain rate tensor. $Re \geq 1$ is the Reynolds number, $Re \equiv LU\rho/\eta_0$, in which η_0 is the zero-shear-rate viscosity, L and U are characteristic length and velocity, respectively, and ρ is the density. $\widehat{\mathbf{f}}$ is the body force vector, the unknowns $\mathbf{u}$ and $\boldsymbol{\tau}$ are the velocity and the extra-stress tensor, respectively, and p is the scalar pressure. We assume that the pressure p satisfies a zero mean constraint,

$$\int_\Omega p dx = 0,$$

in order to ensure the uniqueness of pressure; see [5]. As for the system (2.1), it was illustrated in [14] that the system is suitable for incompressible non-Newtonian flows when a direct approximation of the extra-stress tensor is desired.

Let $\dot{\gamma}(\mathbf{u}) = \sqrt{2\left(\mathbf{D}(\mathbf{u}) : \mathbf{D}(\mathbf{u})\right)}$ be the shear rate with the double-dot product between two second-order tensors $\boldsymbol{\tau}$ and $\boldsymbol{\sigma}$ defined as

$$\boldsymbol{\tau} : \boldsymbol{\sigma} = \sum_{i,j} \tau_{ij}\sigma_{ji}.$$

We implement the generalized Newtonian fluid equation known as the Carreau model [4], i.e.,

$$\eta(\dot{\gamma}(\mathbf{u})) = \eta_0[1 + (\lambda_c\dot{\gamma}(\mathbf{u}))^2]^{\frac{n-1}{2}}, \tag{2.2}$$

where λ_c is a Carreau time constant and n is a power law exponent. In the case of $n = 1$, the model reduces to the linear Newtonian model, the Navier−Stokes equations. For a shear-thinning fluid, n is less than one, which means that the viscosity decreases by increasing shear rate. For large values of $\dot{\gamma}$, the Ostwald−de Waele power−law function is recovered with the consistency index, K, corresponding to $\eta_0\lambda_c^{n-1}$ [3]. The Carreau model is commonly used for modeling blood flow [25] and describes the shearing viscosity of polymer melts that exhibit a Newtonian behavior at low strain rates followed by a power-law behavior for increasing strain rates [26].

3. Notation and preliminaries. Typically, the solution of the nonlinear Navier−Stokes equations using the Carreau model in (2.1) is approximated by a sequence of the linearized Navier−Stokes equations which is formulated in this section. Each intermediate, linear step is discretized by minimizing a least-squares finite element functional. In this section we describe the function spaces for the unknowns, the least-squares minimization, and the ellipticity of the least-squares finite element functional. The nonlinear iteration is discussed in detail in section 4.

Let $\mathcal{D}(\Omega)$ be the linear space of infinitely differentiable functions with compact supports on Ω, that is,

$$\mathcal{D}\left(\bar{\Omega}\right) = \{\psi|_\Omega : \psi \in \mathcal{D}(\mathcal{O}) \text{ for some open subsect } \Omega \subset \mathcal{O} \subset \mathbb{R}^2\};$$

see [31]. Let $H^s(\Omega)$, $s \geq 0$, be the Sobolev spaces with the standard associated inner products $(\cdot,\cdot)_s$ and their respective norms $\|\cdot\|_s$. For $s = 0$, $H^s(\Omega)$ coincides with $L^2(\Omega)$, and $H_0^s(\Omega)$ denotes the closure of $\mathcal{D}(\Omega)$ with respect to the norm $\|\cdot\|_s$. For positive values of s, the space $H^{-s}(\Omega)$ is defined as the dual space of $H_0^s(\Omega)$ equipped with the norm

$$\|\sigma\|_{-s} := \sup_{0\neq v\in H_0^s(\Omega)} \frac{(\sigma, v)}{\|v\|_s},$$

where $(.,.)$ is the duality pairing between $H^{-s}(\Omega)$ and $H_0^s(\Omega)$ when there is no risk of confusion. Let $\mathbf{H}(\mathrm{div};\Omega) = \upsilon \in \mathbf{L}^2(\Omega)^2 : \nabla\cdot\upsilon \in L^2(\Omega)$ with the respective norm $\|\upsilon\|_{\mathbf{H}(\mathrm{div};\Omega)} := (\|\upsilon\|_0^2 + \|\nabla\cdot\upsilon\|_0^2)^{\frac{1}{2}}$.

The function spaces used in our variational formulations are defined as

$$\begin{aligned} \boldsymbol{V} &:= \{\mathbf{v} \mid \mathbf{v} \in \mathbf{H}^1(\Omega)^2,\ \mathbf{v} = \mathbf{0} \text{ on } \partial\Omega\},\\ Q &:= \{q \mid q \in L^2(\Omega), \int_\Omega q dx = 0\},\\ \boldsymbol{\Sigma}_s &:= \{\boldsymbol{\sigma} \mid \boldsymbol{\sigma} \in \mathbf{L^2}(\Omega)^2,\ \sigma_{ij} = \sigma_{ji}\}, \end{aligned}$$

and let the product space $\Phi := \boldsymbol{V} \times Q \times \boldsymbol{\Sigma}_s$.

Based on [20], linearizing (2.1) about the approximation

$$\mathbf{u}_0 \approx \mathbf{u},$$

where we assume $\triangledown\cdot\mathbf{u}_0 = 0$ and

$$M := \max\{\|\mathbf{u}_0\|_\infty,\ \|\nabla\mathbf{u}_0\|_\infty\} < \infty, \tag{3.1}$$

results in the following replacement rules:

$$\mathbf{u}\cdot\nabla\mathbf{u} \approx \mathbf{u}_0\cdot\nabla\mathbf{u} + \mathbf{u}\cdot\nabla\mathbf{u}_0 - \mathbf{u}_0\cdot\nabla\mathbf{u}_0,$$

$$\eta(\dot{\gamma}(\mathbf{u}))\mathbf{D}(\mathbf{u}) \approx \eta(\dot{\gamma}(\mathbf{u}_0))\mathbf{D}(\mathbf{u}) + \eta(\dot{\gamma}(\mathbf{u}))\mathbf{D}(\mathbf{u}_0) - \eta(\dot{\gamma}(\mathbf{u}_0))\mathbf{D}(\mathbf{u}_0),$$

and

$$\eta(\dot{\gamma}(\mathbf{u}_0)) \approx \eta_0.$$

As stated in [4], we apply Newton's method to the nonlinear viscosity equation (2.2). Let $\mathbf{u} = \tilde{\mathbf{u}} + \mathbf{u}_0$, where $\mathbf{u}_0$ is the initial guess and $\tilde{\mathbf{u}}$ is the correction in the Newton iteration. A binomial expansion of $\eta\left(\dot{\gamma}(\mathbf{u}_0 + \varepsilon\tilde{\mathbf{u}})\right)$ yields the equation

$$\eta\left(\dot{\gamma}(\mathbf{u}_0 + \varepsilon\tilde{\mathbf{u}})\right) = \eta\left(\dot{\gamma}(\mathbf{u}_0)\right)\left[1 + \varepsilon G\left(\mathbf{u}_0, \tilde{\mathbf{u}}\right) + O\left(\varepsilon^2\right)\right], \tag{3.2}$$

where

$$G\left(\mathbf{u_0}, \tilde{\mathbf{u}}\right) = 2(n-1)\lambda_c^2 \frac{\mathbf{D}(\mathbf{u}_0) : \mathbf{D}(\tilde{\mathbf{u}})}{1 + \lambda_c^2[\dot{\gamma}(\mathbf{u}_0)]^2}. \tag{3.3}$$

Hence,

$$\eta\left(\dot{\gamma}(\mathbf{u})\right) \approx \eta_0\left[1 + G\left(\mathbf{u}_0, \mathbf{u}\right) - G\left(\mathbf{u}_0, \mathbf{u}_0\right)\right]. \tag{3.4}$$

The linearized velocity-pressure-stress system may now be written as

$$\mathbf{u}_0 \cdot \nabla\mathbf{u} + \mathbf{u} \cdot \nabla\mathbf{u}_0 - \nabla \cdot \boldsymbol{\tau} + \nabla p = \mathbf{f} \ \text{ in } \Omega, \tag{3.5}$$

$$\boldsymbol{\tau} - \frac{2}{Re}\mathbf{D}(\mathbf{u}) - \frac{2}{Re}\mathbf{D}(\mathbf{u}_0)G\left(\mathbf{u}_0, \mathbf{u}\right) = \mathbf{g} \ \text{ in } \Omega, \tag{3.6}$$

$$\nabla \cdot \mathbf{u} = 0 \ \text{ in } \Omega, \tag{3.7}$$

$$\mathbf{u} = \mathbf{0} \ \text{ on } \Gamma, \tag{3.8}$$

where we define

$$\mathbf{f} = \mathbf{u}_0 \cdot \nabla\mathbf{u}_0 + \widehat{\mathbf{f}},$$
$$\mathbf{g} = \frac{-2}{Re}\mathbf{D}(\mathbf{u}_0)G\left(\mathbf{u}_0, \mathbf{u}_0\right).$$

The least-squares functional for (3.5)−(3.8) we consider is given by

$$\begin{aligned} J(\mathbf{u}, p, \boldsymbol{\tau}; \mathbf{F}) = {} & \|\mathbf{u}_0 \cdot \nabla\mathbf{u} + \mathbf{u} \cdot \nabla\mathbf{u}_0 - \nabla \cdot \boldsymbol{\tau} + \nabla p - \mathbf{f}\|_0^2 \\ & + \left\|\boldsymbol{\tau} - \frac{2}{Re}\mathbf{D}(\mathbf{u}) - \frac{2}{Re}\mathbf{D}(\mathbf{u}_0)G\left(\mathbf{u}_0, \mathbf{u}\right) - \mathbf{g}\right\|_0^2 + KRe^{-2}\|\nabla \cdot \mathbf{u}\|_0^2, \end{aligned} \tag{3.9}$$

where the weight Re^{-2} is considered based on the inertial term. The positive mass conservation constant K is chosen based on similar considerations as those used in [15, 4, 16]. The results indicate that least-squares solutions can be improved by sufficiently scaling the mass conservation term. Note that weighting the divergence term with Re^{-2} will put less weight on this when the Reynolds number is large. To solve the problem, we denote the nonlinear least-squares functional of the residual of the system (2.1) as follows:

$$g(\mathbf{u}, p, \boldsymbol{\tau}; \widehat{\mathbf{f}}) := \left\|\mathbf{u} \cdot \nabla\mathbf{u} - \nabla \cdot \boldsymbol{\tau} + \nabla p - \widehat{\mathbf{f}}\right\|_0^2 + \left\|\boldsymbol{\tau} - \frac{2\eta\left(\dot{\gamma}(\mathbf{u})\right)\mathbf{D}(\mathbf{u})}{\eta_0 Re}\right\|_0^2 + \|\nabla \cdot \mathbf{u}\|_0^2. \tag{3.10}$$

The nonlinear L^2 functional is a posteriori error estimates for first-order system least-squares finite element methods as in [19, 21] and serves as an indicator to adjust the weight $K = 10^m$,

where m ranges from 1 to 8 in (3.9). Note that the ranges of m vary with the problems and the computational domain in [15, 27]. The practicality of the proposed a posteriori error estimates for adjusting the weight of the divergence term will be shown in section 6, and then numerical results show that the weight Re^{-2} would not hurt the mass conservation in the system when the Reynolds number is large. However, the weight K is set to one here for the convenience of the analysis.

Denote two norms as

$$|||(\mathbf{u},p,\boldsymbol{\tau})||| = \left(\|\boldsymbol{\tau}\|_0^2 + \|p\|_0^2 + \frac{1}{Re^2}\|\mathbf{u}\|_1^2 \right)^{1/2}$$

and

$$|||(\mathbf{u},p,\boldsymbol{\tau})|||_1 = \left(\|\boldsymbol{\tau}\|_1^2 + \|p\|_1^2 + \frac{1}{Re^2}\|\mathbf{u}\|_1^2 \right)^{1/2}$$

over Φ. Note that Kim and Shin [23] presented an H^{-1}-norms least-squares method for the Stokes equations with the stress tensor $\boldsymbol{\tau} = 2\mathbf{D}(\mathbf{u})/Re$ and established the following a priori estimate:

$$C|||(\mathbf{u},p,\boldsymbol{\tau})|||^2 \le \left\| \boldsymbol{\tau} - \frac{2}{Re}\mathbf{D}(\mathbf{u}) \right\|_0^2 + \frac{1}{Re^2}\|\nabla\cdot\mathbf{u}\|_0^2 + \|-\nabla\cdot\boldsymbol{\tau} + \nabla p\|_{-1}^2, \tag{3.11}$$

where a constant $C > 0$ is independent of Re, $\forall(\mathbf{u},p,\boldsymbol{\tau}) \in \Phi$.

We now derive some a priori estimates for the first-order system (3.5), i.e., the coercivity and continuity estimates for the homogeneous least-squares functional. The a priori estimates identify the dependence of the estimate on the Reynolds number Re and will play crucial roles in the error estimates of our least-squares finite element method.

Theorem 1. For any $(\mathbf{u},p,\boldsymbol{\tau}) \in \Phi$, there are positive constants, c_0 and c_1, which depend on Ω, n, λ_c, and M in (3.1), such that

$$c_0|||(\mathbf{u},p,\boldsymbol{\tau})|||^2 \le J(\mathbf{u},p,\boldsymbol{\tau};\mathbf{0}) \le c_1|||(\mathbf{u},p,\boldsymbol{\tau})|||_1^2 \tag{3.12}$$

for sufficiently small M in Ω satisfying

$$M \le \frac{1}{2Re}. \tag{3.13}$$

Proof.
Let $(\mathbf{u},p,\boldsymbol{\tau}) \in \Phi$. The upper bound follows naturally from the triangle inequality and (3.13). We proceed to show the validity of the lower bound in (3.12). By the continuity of the embedding $L^2(\Omega) \subset H^{-1}(\Omega)$, using the inequality $\|a+b\|^2 \ge (1/2)\|a\|^2 - |b\|^2$ and the estimate

(3.11), we have

$$
\begin{aligned}
&J(\mathbf{u},p,\boldsymbol{\tau};\mathbf{0})\\
&\geq \left\|\boldsymbol{\tau}-\frac{2}{Re}\mathbf{D}(\mathbf{u})-\frac{2}{Re}\mathbf{D}(\mathbf{u}_0)G(\mathbf{u_0},\mathbf{u})\right\|_0^2+\frac{1}{Re^2}\|\nabla\cdot\mathbf{u}\|_0^2\\
&+\|-\nabla\cdot\boldsymbol{\tau}+\nabla p+\mathbf{u}_0\cdot\nabla\mathbf{u}+\mathbf{u}\cdot\nabla\mathbf{u}_0\|_{-1}^2\\
&\geq \left\|\boldsymbol{\tau}-\frac{2}{Re}\mathbf{D}(\mathbf{u})-\frac{2}{Re}\mathbf{D}(\mathbf{u}_0)G(\mathbf{u_0},\mathbf{u})\right\|_0^2+\frac{1}{Re^2}\|\nabla\cdot\mathbf{u}\|_0^2+\frac{1}{2}\|-\nabla\cdot\boldsymbol{\tau}+\nabla p\|_{-1}^2\\
&-\|\mathbf{u}_0\cdot\nabla\mathbf{u}+\mathbf{u}\cdot\nabla\mathbf{u}_0\|_{-1}^2\\
&\geq \frac{1}{2}\left(\left\|\boldsymbol{\tau}-\frac{2}{Re}\mathbf{D}(\mathbf{u})\right\|_0^2+\frac{1}{Re^2}\|\nabla\cdot\mathbf{u}\|_0^2+\|-\nabla\cdot\boldsymbol{\tau}+\nabla p\|_{-1}^2\right)-\frac{4\|\mathbf{D}(\mathbf{u}_0)\|_0^2}{Re^2}\|G(\mathbf{u_0},\mathbf{u})\|_0^2\\
&-\|\mathbf{u}_0\cdot\nabla\mathbf{u}+\mathbf{u}\cdot\nabla\mathbf{u}_0\|_0^2\\
&\geq \frac{1}{2}\left(\left\|\boldsymbol{\tau}-\frac{2}{Re}\mathbf{D}(\mathbf{u})\right\|_0^2+\frac{1}{Re^2}\|\nabla\cdot\mathbf{u}\|_0^2+\|-\nabla\cdot\boldsymbol{\tau}+\nabla p\|_{-1}^2\right)-C_1(n-1)^2\lambda_c^4Re^{-2}M^4\|\mathbf{u}\|_1^2-C_2M^2\|\mathbf{u}\|_1^2\\
&\geq C_3\left(\|\boldsymbol{\tau}\|_0^2+\|p\|_0^2+\frac{1}{Re^2}\|\mathbf{u}\|_1^2-\frac{1}{Re^2}M^4\|\mathbf{u}\|_1^2-M^2\|\mathbf{u}\|_1^2\right)\\
&\geq C_3\left(\|\boldsymbol{\tau}\|_0^2+\|p\|_0^2+\frac{1}{Re^2}\|\mathbf{u}\|_1^2\left(1-M^4-Re^2M^2\right)\right).
\end{aligned}
$$

By using (3.13), we have $1-M^4-Re^2M^2>0$. Hence,

$$J(\mathbf{u},p,\boldsymbol{\tau};\mathbf{0})\geq c_0\,|||(\mathbf{u},p,\boldsymbol{\tau})|||^2$$

for some positive constant c_0 which is independent of Re.

□

Therefore, the coercivity and continuity estimates of the functional $J(\mathbf{u},p,\boldsymbol{\tau};\mathbf{0})$ have been established in Theorem 1. The least-squares minimization problem for the solution of system (3.5)−(3.8) is to choose $(\mathbf{u},p,\boldsymbol{\tau})\in\Phi$ such that

$$J(\mathbf{u},p,\boldsymbol{\tau};\mathbf{F})=\inf_{(\mathbf{v},q,\boldsymbol{\sigma})\in\Phi}J(\mathbf{v},q,\boldsymbol{\sigma};\mathbf{F}). \tag{3.14}$$

4. Finite element approximation. For the finite element approximation, we assume that the domain Ω is a polygon and that $\mathcal{T}_h$ is a partition of Ω into finite elements $\Omega=\bigcup_{T\in\mathcal{T}_h}T$ with $h=\max\{\mathrm{diam}(T):T\in\mathcal{T}_h\}$. Assume that the triangulation $\mathcal{T}_h$ is regular and satisfies the inverse assumption (see [23]). The grid size is defined as $h=2\sqrt{A}/\sqrt{N}$, where A is the area of the domain and N is the number of elements in $\mathcal{T}_h$. Let $P_r(T)$ denote the standard space of degree r polynomials on element T. Define finite element spaces for the approximate of ($\mathbf{u}$, p, $\boldsymbol{\tau}$):

$$
\begin{aligned}
\boldsymbol{V}^h&=\{\mathbf{v}^h\mid\mathbf{v}^h\in\mathbf{V}\cap(C^0(\Omega))^2,\ \mathbf{v}^h|_T\in P_{r+1}(T)^2\ \forall T\in\mathcal{T}_h\},\\
Q^h&=\{q^h\mid q^h\in Q\cap C^0(\Omega),\ q^h|_T\in P_{r+1}(T)\ \forall T\in\mathcal{T}_h\},\\
\boldsymbol{\Sigma}_s^h&=\{\boldsymbol{\sigma}^h\mid\boldsymbol{\sigma}^h\in\boldsymbol{\Sigma}_s\cap(C^0(\Omega))^{2\times2},\ \boldsymbol{\sigma}^h|_T\in P_{r+1}(T)^{2\times2}\ \forall T\in\mathcal{T}_h\}.
\end{aligned}
$$

Let $\Phi^h:=\mathbf{V}^h\times Q^h\times\boldsymbol{\Sigma}_s^h$ be finite element subspaces of Φ with the following approximation prosperities. Let $S^h=\{u\in C^0(\Omega):u|_T\in P_{r+1}(T)\ \forall T\in\mathcal{T}_h\}$ admit the property

$$\inf_{u^h\in S^h}\left\|u-u^h\right\|_l\leq Ch^m\|u\|_{m+l}\,\forall u\in H^{m+l}(\Omega), \tag{4.1}$$

for $l = 0, 1$.

The discrete minimization problem is to choose $(\mathbf{u}^h, p^h, \boldsymbol{\tau}^h) \in \Phi^h$ such that

$$J(\mathbf{u}^h, p^h, \boldsymbol{\tau}^h; \mathbf{F}) = \inf_{(\mathbf{v}^h, q^h, \boldsymbol{\sigma}^h) \in \Phi^h} J(\mathbf{v}^h, q^h, \boldsymbol{\sigma}^h; \mathbf{F}). \tag{4.2}$$

Then the finite element approximation to (4.2) is equivalent to seek for $(\mathbf{u}^h, p^h, \boldsymbol{\tau}^h) \in \Phi^h$ such that

$$\mathfrak{B}((\mathbf{u}^h, p^h, \boldsymbol{\tau}^h); (\mathbf{v}^h, q^h, \boldsymbol{\sigma}^h)) = \mathfrak{F}((\mathbf{v}^h, q^h, \boldsymbol{\sigma}^h)) \tag{4.3}$$

$\forall (\mathbf{v}^h, q^h, \boldsymbol{\sigma}^h) \in \Phi^h$, where

$$\begin{aligned}
&\mathfrak{B}((\mathbf{u}^h, p^h, \boldsymbol{\tau}^h); (\mathbf{v}^h, q^h, \boldsymbol{\sigma}^h)) \\
&= \int_\Omega \left(\mathbf{u}_0 \cdot \nabla \mathbf{u}^h + \mathbf{u}^h \cdot \nabla \mathbf{u_0} - \nabla \cdot \boldsymbol{\tau}^h + \nabla p^h \right) \cdot \left(\mathbf{u}_0 \cdot \nabla \mathbf{v}^h + \mathbf{v}^h \cdot \nabla \mathbf{u_0} - \nabla \cdot \boldsymbol{\sigma}^h + \nabla q^h \right) d\Omega \\
&+ \int_\Omega \left(\boldsymbol{\tau}^h - \frac{2}{Re}\mathbf{D}(\mathbf{u}^h) - \frac{2}{Re}\mathbf{D}(\mathbf{u}_0) G\left(\mathbf{u_0}, \mathbf{u^h}\right) \right) : \left(\boldsymbol{\sigma}^h - \frac{2}{Re}\mathbf{D}(\mathbf{v}^h) - \frac{2}{Re}\mathbf{D}(\mathbf{u}_0) G\left(\mathbf{u_0}, \mathbf{v}^h\right) \right) d\Omega \\
&+ KRe^{-2} \int_\Omega (\nabla \cdot \mathbf{u}^h)(\nabla \cdot \mathbf{v}^h) d\Omega,
\end{aligned}$$

and

$$\begin{aligned}
&\mathfrak{F}((\mathbf{v}^h, q^h, \boldsymbol{\sigma}^h)) \\
&= \int_\Omega \mathbf{f} \cdot \left(\mathbf{u}_0 \cdot \nabla \mathbf{v}^h + \mathbf{v}^h \cdot \nabla \mathbf{u}_0 - \nabla \cdot \boldsymbol{\sigma}^h + \nabla q^h \right) + \mathbf{g} \cdot \left(\boldsymbol{\sigma}^h - \frac{2}{Re}\mathbf{D}(\mathbf{v}^h) - \frac{2}{Re}\mathbf{D}(\mathbf{u}_0) G\left(\mathbf{u}_0, \mathbf{v}^h\right) \right) d\Omega.
\end{aligned}$$

Since Φ^h is a finite element subspace of Φ, using arguments similar to those in [15] and [28], and Theorem 1, the Lax−Milgram lemma, and (4.3), the following theorem is proved.

Theorem 2. Suppose assumptions (3.1) and (3.13) hold. The least-squares functional (3.9) has a unique solution $(\mathbf{u}^h, p^h, \boldsymbol{\tau}^h) \in \Phi^h$ for any h, and the solution satisfies the following stability estimate:

$$\left| \left| \left| (\mathbf{u}^h, p^h, \boldsymbol{\tau}^h) \right| \right| \right| \leq \left(\|\mathbf{f}\|_0 + \|\mathbf{g}\|_0 \right). \tag{4.4}$$

Moreover, the matrix of the linear algebraic system associated with the least-squares scheme (4.3) is symmetric and positive definite.

We now give error estimates for the solution to (4.2). Using similar arguments in [20], Theorem 1, and the approximation properties (4.1), the following error estimate is established.

Theorem 3. Consider approximating the solution to (3.5)-(3.8) through the discrete minimization problem (4.2) under the assumptions in (3.1) and (3.13). Assume that $(\mathbf{u}, p, \boldsymbol{\tau}) \in \Phi$ is the solution to (3.14); then the solution to (4.2) satisfies

$$\left| \left| \left| (\mathbf{u} - \mathbf{u}^h, p - p^h, \boldsymbol{\tau} - \boldsymbol{\tau}^h) \right| \right| \right| \leq C h^m \left(\|\boldsymbol{\tau}\|_{m+1} + \|p\|_{m+1} + \frac{1}{Re} \|\mathbf{u}\|_{m+1} \right) \tag{4.5}$$

for $m \leq r + 1$.

Proof.
Theorem 1 directly leads to the bound

$$\left|\left|\left|(\mathbf{u}-\mathbf{u}^h, p-p^h, \boldsymbol{\tau}-\boldsymbol{\tau}^h)\right|\right|\right| \leq \inf_{(\mathbf{v}^h,q^h,\boldsymbol{\sigma}^h)\in\boldsymbol{\Phi}^h} \frac{c_1}{c_0}\left|\left|\left|(\mathbf{u}-\mathbf{v}^h, p-q^h, \boldsymbol{\tau}-\boldsymbol{\sigma}^h)\right|\right|\right|_1,$$

which, using the approximation properties in (4.1), yields the desired error bound for $m \leq r+1$.

□

The results of the stress formulation are similar to works on the convergence of the velocity-vorticity-pressure least-squares method for linearized Navier−Stokes equations governing the Oseen problem by Tsai and Yang [28]. Note that the use of continuous piecewise linear polynomials for all unknowns yields the error estimates

$$\left|\left|\left|(\mathbf{u}-\mathbf{u}^h, p-p^h, \boldsymbol{\tau}-\boldsymbol{\tau}^h)\right|\right|\right| \leq Ch\left(\|\boldsymbol{\tau}\|_2 + \|p\|_2 + \frac{1}{Re}\|\mathbf{u}\|_2\right). \tag{4.6}$$

We expect the following rates:

$$\|\boldsymbol{\tau}-\boldsymbol{\tau}^h\|_0 = O(h),\ \|p-p^h\|_0 = O(h), \text{and } \|\mathbf{u}-\mathbf{u}^h\|_1 = O(h).$$

The theoretically predicted error bounds are only $O(h)$ in the L^2-norm for p and $\boldsymbol{\tau}$ and $O(h)$ in the H^1-norm for $\mathbf{u}$. Hence, we have the optimal convergence rate of the velocity in the H^1-norm and suboptimal convergence rates of the stress and pressure in the L^2-norm.

Finally, we end this section by detailing the procedure of the Newton iteration scheme for solving the Navier−Stokes equations with the Carreau model (2.1) using the least-squares approach. The solution of the nonlinear Navier−Stokes systems in (2.1) was approximated by a sequence of the linearized velocity-pressure-stress system (3.5)−(3.8). The least-squares approach to the linearized system (3.5)−(3.8) provided an iterative procedure as follows.

We give an initial approximation $(\mathbf{u}_0^h, p_0^h, \boldsymbol{\tau}_0^h)$ and then attempt to seek approximations $(\mathbf{u}_{\ell+1}^h, p_{\ell+1}^h, \boldsymbol{\tau}_{\ell+1}^h) \in \boldsymbol{\Phi}^h$ for $\ell = 0,\ 1,\ 2,\ \ldots$ satisfying

$$J_\ell(\mathbf{u}_{\ell+1}^h, p_{\ell+1}^h, \boldsymbol{\tau}_{\ell+1}^h; \mathbf{F}) = \inf_{(\mathbf{v}^h,q^h,\boldsymbol{\sigma}^h)\in\boldsymbol{\Phi}^h} J_\ell(\mathbf{v}^h, q^h, \boldsymbol{\sigma}^h; \mathbf{F}), \tag{4.7}$$

where the least-squares functional $J_\ell(\mathbf{u}, p, \boldsymbol{\tau}; \mathbf{F})$ is defined as

$$\begin{aligned} J_\ell(\mathbf{u}, p, \boldsymbol{\tau}; \mathbf{F}) = &\left\|\mathbf{u}_\ell^h\cdot\nabla\mathbf{u} + \mathbf{u}\cdot\nabla\mathbf{u}_\ell^h - \nabla\cdot\boldsymbol{\tau} + \nabla p - \mathbf{f}\right\|_0^2 \\ &+ \left\|\boldsymbol{\tau} - \frac{2}{Re}\mathbf{D}(\mathbf{u}) - \frac{2}{Re}\mathbf{D}(\mathbf{u}_\ell^h)G\left(\mathbf{u}_\ell^h, \mathbf{u}\right) - \mathbf{g}\right\|_0^2 + KRe^{-2}\|\nabla\cdot\mathbf{u}\|_0^2, \end{aligned} \tag{4.8}$$

where

$$\begin{aligned} \mathbf{f} &= \mathbf{u}_\ell^h\cdot\nabla\mathbf{u}_\ell^h + \widehat{\mathbf{f}}, \\ \mathbf{g} &= \frac{-2}{Re}\mathbf{D}(\mathbf{u}_\ell^h)G\left(\mathbf{u}_\ell^h, \mathbf{u}_\ell^h\right), \end{aligned}$$

over the space $\boldsymbol{\Phi}$.

5. The adaptively refined algorithm for flow problems. Adaptive grids aligned with high gradient regions are often necessary to reduce the size of the linearized system of equations and to resolve the singularities arising from geometric discontinuities. In our previous work [22], adaptive least-squares finite element methods for viscoelastic flow problems were developed. The idea is to adjust the position of the grid points and produce a mesh with the same number of unknowns, which is more aptly graded for the given problem. In [22], results indicated that the graded meshes agree with the physical attributes of these models and smoothed triangulation can improve convergence rates and errors. However, grid effects of nonuniform meshes were also reported in [22] for the NWLS method using lower-order basis functions. Unlike previous research [22], we developed a new adaptive algorithm, which adds new grids on the high gradient region, but does not adjust the position of the original mesh. The advantage of this method is that it maintains the accuracy of the low gradient region, which has low accuracy in previous methods in which grids are moved toward high gradient regions. We itemize an adaptive algorithm to construct refined grids of the least-squares approximations for our model equations (3.5)-(3.8) as follows:

1. Select initial grids, e.g., quasi-uniform grids.
2. Triangulate the point set by a Delaunay grid generation technique considered by Shewchuk [29] and produce a mesh $\mathcal{T}$ with elements T. Solve the problem by the finite element method.
3. Compute the grading function
$$\phi_T = |R(\nabla q)|_T, \tag{5.1}$$
where R is a gradient recovery technique employed to compute the gradient of the scalar q. Our implementation follows from [24] by defining an average type recovery scheme $R : \nabla\mathbb{V}_N \mapsto \bar{\mathbb{V}}_N \times \bar{\mathbb{V}}_N$ with
$$R(\nabla q_N)(x_i) = \frac{\sum_{T\in w_i} |T||\nabla q_N|_T}{|w_i|}, \tag{5.2}$$
where for all vertices $x_i \in \mathcal{T}$, w_i is the patch including the vertices x_i, that is, the union of all triangles contain x_i, and $|\cdot|$ is the two-dimensional Lebesgue measure.
4. Compute the mesh redistribution function $f(\phi_T)$, where f is defined by
$$f(\phi_T) = |T|_{max} - (\phi_T - \phi_{T_{min}})\,\frac{\Delta|T|}{\Delta\phi_T},$$
where $|T|_{max} = \max\{|T| : \forall T \in \mathcal{T}\}$, $\Delta|T| = |T|_{max} - |T|_{min}$, and $\Delta\phi_T = \phi_{T_{max}} - \phi_{T_{min}}$.
5. If $T \in \mathcal{T}$ satisfies $f(\phi_T) < |T|$, then T is subdivided.
6. Update the grid point information. Continue to step 2 to triangulate the point set, check if the stopping criterion (the variation of the minimum h between consecutive iterations is less than some prescribed tolerance) is satisfied, and repeat the process if not.

Note that the least-squares method in (3.9) is used in step 2, and all the computations are performed using linear interpolation for all unknowns. The least-squares method is simpler to implement than either the GLS or the NWLS method. In step 3, the grading function ϕ_T that varies with the scalar q in (5.1) is used to generate the required refined nodes in the computational domain. To illustrate the capability of the algorithm, adaptive mesh refinements on the square test domain are performed in Section 6 on three scalars q, where velocity magnitude $|\mathbf{u}|_2 = \sqrt{\mathbf{u}_x^2 + \mathbf{u}_y^2}$, stress magnitude $|\boldsymbol{\tau}|_2 = \sqrt{\boldsymbol{\tau}_{xx}^2 + \boldsymbol{\tau}_{yy}^2 + \boldsymbol{\tau}_{xy}^2}$, and pressure is $|p|$. Note that the choice of q depends on the physical property of the flows that we are concerned with. For the 4-to-1 contraction domain, the velocity magnitude is used to illustrate the effectiveness and robustness of the algorithm.

6. Numerical results. The governing equations are solved on two domains in this section. The first domain is a square test domain with exact boundary conditions used to measure convergence rates. The second is the 4-to-1 contraction channel problem consisting of an upstream channel that abruptly narrows to a channel one quarter of the original width. These domains with boundaries are shown in Figure 6.1.

For the first test domain, the boundary conditions are as follows:

$$\mathbf{u} = \mathbf{u}_\Gamma \quad \text{on} \quad \Gamma_{in},\ \Gamma_{wall},\ \Gamma_{out}, \tag{6.1}$$

$$p = p_0 \quad \text{on} \quad \Gamma_{out} \cap \Gamma_{sym}, \tag{6.2}$$

$$\mathbf{u}\cdot\mathbf{n} = 0,\ \boldsymbol{\pi} : \mathbf{nt} = 0 \quad \text{on} \quad \Gamma_{sym}. \tag{6.3}$$

For the 4-to-1 contraction domain, let $\mathbf{u} = (u, v)$, which includes the following boundary conditions:

$$\mathbf{u} = \mathbf{u}_\Gamma \quad \text{on} \quad \Gamma_{in}, \tag{6.4}$$

$$\mathbf{u} = \mathbf{0} \quad \text{on} \quad \Gamma_{wall}, \tag{6.5}$$

$$v = 0,\ p = 0 \quad \text{on} \quad \Gamma_{out}, \tag{6.6}$$

$$\mathbf{u}\cdot\mathbf{n} = 0,\ \boldsymbol{\pi} : \mathbf{nt} = 0 \quad \text{on} \quad \Gamma_{sym}. \tag{6.7}$$

Note that $\mathbf{n}$ and $\mathbf{t}$ are unit vectors outward normal and tangent to the boundary, respectively. $\boldsymbol{\pi} = p\boldsymbol{I} - \boldsymbol{\tau}$ is the Cauchy stress tensor, and $\mathbf{u}_\Gamma$ and $\boldsymbol{\tau}_\Gamma$ are specified boundary functions. These boundary conditions are also used in [15].

Our method couples the least-squares functional (4.8) with adaptive mesh refinement. The resulting linear algebraic system of equations with a symmetric positive define coefficient matrix is solved using the Gaussian elimination method. Convergence of the iteration scheme in (4.7) was declared when the relative norm of the residual in velocities, $\|\mathbf{u}^h_{\ell+1} - \mathbf{u}^h_\ell\|/\|\mathbf{u}^h_{\ell+1}\|$, between two consecutive iterations was less than 10^{-4}. Both cases presented here use linear basis functions for all variables. Previous studies [11] showed that mass conservation is not favorable in least-squares based formulations when low-order basis functions are used. To properly adjust the weights $K = 10^m$ in (4.8), we iterate on m, where m ranges from 1 to 8, to determine approximate convergence of the functional $g^{1/2}$ in (3.10). The functional $g^{1/2}$ is used as a posteriori error estimates for the first-order system least-squares finite element method. Note that the ranges of m vary with the problems and the computational domain in [15] and [27]. In addition, the functional $g^{1/2}$ is also used in a refinement process to illustrate convergence of the method. Based on [20, 21, 30], under certain smoothness assumptions, the following error bound is used to estimate the functional which is equivalent to the H^1-norm [31]:

$$g^{1/2}(\mathbf{u}^h, p^h, \boldsymbol{\tau}^h; \widehat{\mathbf{f}}) \approx \left(\|\mathbf{u} - \mathbf{u}^h\|_1^2 + \|p - p^h\|_1^2 + \|\boldsymbol{\tau} - \boldsymbol{\tau}^h\|_1^2 \right)^{1/2} \leq Ch\left(\|\boldsymbol{\tau}\|_2 + \|p\|_2 + \|\mathbf{u}\|_2\right).$$

Thus, for the finite element space used here, optimal convergence implies $g^{1/2} = O(h)$.

We provide numerical results for the Navier−Stokes equations using the Carreau model (2.1) by using the iteration schemes (4.7). Each iteration involved the linearized velocity-pressure-stress Navier−Stokes equations (3.5)-(3.8) which were analyzed in section 4. However, the results for the linearized velocity-pressure-stress system provided guidance on what the optimal rates would be. It was reasonable to expect that convergence rates of the least-squares approximations for the Navier−Stokes equations using the Carreau model were similar to those for the linearized velocity-pressure-stress system. The least-squares solution of the linearized velocity-pressure-stress system predicted discretization error bounds as $O(h)$

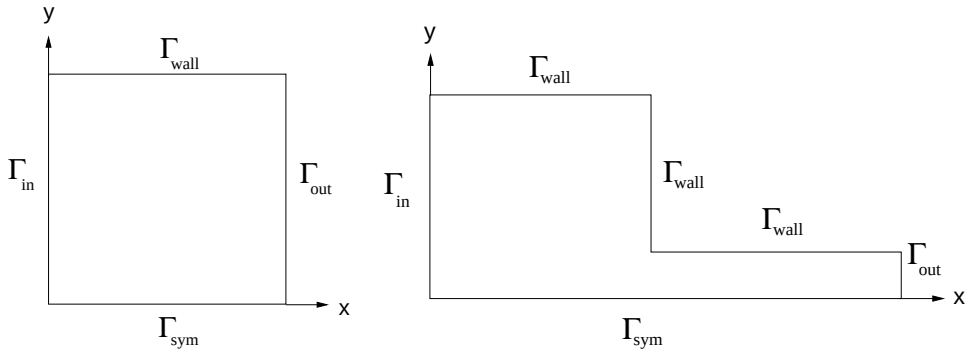

(a) Square test domain (b) 4-to-1 contraction domain

FIG. 6.1. *Computational domains.*

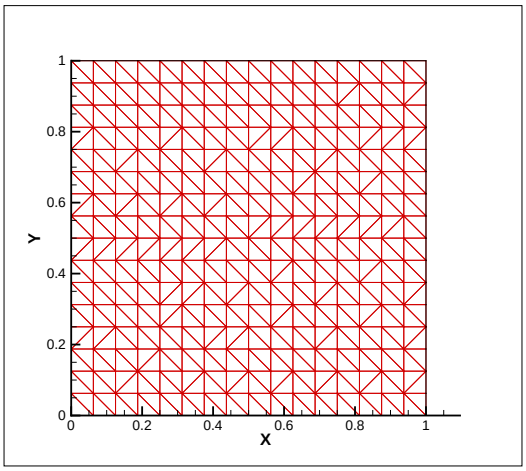

FIG. 6.2. *Mesh D is a uniform directional Delaunay triangular mesh corresponding to* $h = \frac{1}{16}$.

in the L^2-norm for p and τ and as $O(h)$ in the H^1-norm of $O(h)$ for $\mathbf{u}$ by using continuous piecewise linear elements for all variables. Although suboptimal convergence rates in p and τ are obtained in our analysis for the least-squares method using continuous piecewise linear elements for all variables, we show that the optimal convergence rates of $O(h^2)$ in the L^2-norm for all variables can be achieved in the least-squares method using properly refined grids on high gradient regions.

6.1. Example 1: Flow in planar channel. The first problem is the planar channel flow on the square domain $[0,1] \times [0,1]$ considered in [4] with a symmetry line along $y = 0$. The flow domain is shown in Figure 6.1(a). Because of the symmetry along $y = 0$, the computed domain is reduced to half. The exact solutions in Cartesian coordinates are given in [4] by

$$\mathbf{u}_{exact} = \begin{bmatrix} 1 - y^4 \\ 0 \end{bmatrix}$$

and

$$p_{exact} = -x^2.$$

For the square test domain in Figure 6.1(a), the exact solution for the extra-stress tensor is calculated using

$$\boldsymbol{\tau}_{exact} = \frac{1}{\eta_0 Re}\left(2\eta\left(\dot{\gamma}(\mathbf{u}_{exact})\right)\mathbf{D}(\mathbf{u}_{exact})\right).$$

A forcing function, $\mathbf{f}$, must be added to the momentum equation, specifically

$$\mathbf{f} = \begin{bmatrix} \frac{1}{Re}\left(12y^2\left(1+16n\lambda_c^2y^6\right)\left(1+16\lambda_c^2y^6\right)^{\frac{n-3}{2}}\right) - 2x \\ 0 \end{bmatrix}.$$

In the convergence results, the constitutive equation parameters in (2.2) are set as $Re = 1$, $\eta_o = 1$, $n = 0.5$, and $\lambda_c = 1$ for the Carreau model. In the following calculation, the numerical simulation is performed using the two-dimensional incompressible Navier−Stokes equations governing generalized Newtonian flows in the stress based first-order form. We linearize the resulting discrete model using Newton's method.

To illustrate convergence of the method and the influence of the mass conservation in the first problem, we employed three uniform directional Delaunay triangular Meshes D with 8, 16, and 32 partitions per unit length, as shown in Figure 6.2. We list the weight K, the number of elements N, the number of Newton steps, and the nonlinear functional $g^{1/2}$ in Table 6.1. Table 6.1 shows that when $K \geq 100$, for all cases the nonlinear functional norm $g^{1/2}$ is almost consistent, and when $K \geq 10^7$, the iterative process exceeds the maximum number of Newton steps (100) for the case of $N = 2084$. The results show poor conservation of mass is improved by scaling the divergence equation. However, an overweighted divergence equation will worsen the condition of the system, which results in degradation of the performance of the solver, as shown in [13]. In Figure 6.3, we display convergence rates of least-squares solutions using weights ranging from $K = 1$ to $K = 10^8$. The results indicate that the solutions of the cases when $K \geq 100$ are almost identical and that the least-squares solutions containing proper mass conservation weight are improved. Based on our experience using the least-squares method with $K = 100$, the convergence of the functional $g^{1/2}$ and the convergent rates for the least-squares solutions agree well with those of $K \geq 100$. Therefore, it is sufficient to use $K = 100$ for satisfactory results. The mass conservation parameter $K = 100$ is chosen in the least-squares formulations in the example. Note that Figure 6.3 reveals that the best convergence rates in the L^2-norm of the least-squares solutions in which $K = 100$ is used, $\mathbf{u}$, $\boldsymbol{\tau}$, and p are 2.0, 1.4, and 1.3, respectively, and that in the H^1-norm for $\mathbf{u}$ is 1.0. The resulting convergence rates for the velocity are the optimal convergence rates $O(h^2)$ in the L^2-norm and $O(h)$ in the H^1-norm and for the stress and pressure are suboptimal convergence rates $O(h)$ in the L^2-norm. The computed error bounds for the velocity, stress, and pressure agree well with those that are theoretically predicted in section 4.

Next, in Figure 6.2, we consider the directional Delaunay triangular uniform Mesh D with 16 partitions per unit length. The least-squares method based on the adaptively refined algorithm in section 5 (called the AR-NLS method) is performed using initial Mesh D. Refined mesh convergence was declared when the norm of the residual in minimum mesh length between two consecutive iterations was less than 0.01, which required two refined iterations. To understand the influence of the grading functions in our algorithm, we consider three scalars q (5.1) in relation to velocity magnitude $|\mathbf{u}|_2$, stress magnitude $|\boldsymbol{\tau}|_2$, and pressure $|p|$. Convergent adaptively refined Meshes DA, DB and DC are generated by velocity magnitude, stress magnitude, and pressure in Figures 6.4(a), (c), and (e), respectively, and their contours are shown in Figures 6.4(b), (d), and (f), respectively. The results show that Meshes DA, DB, and DC are refined near the wall, near the midpoint of y for the domain, and near the outlet,

	$N = 128$		$N = 512$		$N = 2048$	
Weight K	Steps	$g^{1/2}$	Steps	$g^{1/2}$	Steps	$g^{1/2}$
1	7	0.003095	9	0.000870	10	0.000249
10^1	7	0.003184	9	0.000898	10	0.000257
10^2	6	0.003192	8	0.000906	10	0.000259
10^3	5	0.003187	6	0.000905	9	0.000259
10^4	4	0.003187	6	0.000905	8	0.000260
10^5	4	0.003187	5	0.000905	9	0.000260
10^6	4	0.003187	4	0.000905	22	0.000260
10^7	3	0.003187	4	0.000905	100*	0.000260
10^8	3	0.003187	5	0.000905	100*	0.000260

TABLE 6.1

*Least-squares method on Mesh D for Carreau model at $Re = 1$, $n = 0.5$, and $\lambda_c = 1$. Nonlinear functional norm $g^{1/2}$ in nonlinear nested iteration for various weights K. Here, N denotes the total number of elements and steps mean the number of Newton steps. * indicates the maximum number of Newton steps (100) has been exceeded.*

respectively. These meshes are refined along larger variation areas of the selected variable's magnitude and agree with the physical features of the flow. Accurate velocity profiles are helpful to understand the feature of the flow. Hence, the velocity magnitude gradient is used for the grading refined function in the work.

To illustrate adaptive algorithm capability in the AR-LS solutions, the adaptive refined meshes are generated by Mesh D with 8, 16, and 32 partitions per unit length as initial meshes. The errors of the adaptive mesh refinement solutions are shown in Figure 6.5. The convergence rates in the L^2-norm of the AR-LS solutions for $\mathbf{u}$, $\boldsymbol{\tau}$, and p are 2.8, 2.6, and 2.3, respectively, and in the H^1-norm for $\mathbf{u}$ the convergence rate is 1.5. Note also that the convergence rate of the AR-LS method improves over the least-squares method. In fact, the optimal convergence rates of the AR-least-squares method are obtained in all variables. Based on the results, the convergence rate can be restored using adaptive mesh refinements.

6.2. Example 2: Flow in the 4-to-1 contraction channel. To further show the AR-LS scheme capability for the Carreau model, we applied the method to the 4-to-1 contraction channel in Figure 6.1(b), with x (the flow direction) varying as $-5 \le x \le 5$ and the contraction occurring at $x = 0$. The upstream channel width is 1; thus the downstream width is $1/4$. In our computations, $-5 \le x \le 5$ corresponds to the upstream length $20L$ and the downstream length $20L$, where we use L as the downstream channel width. In the Carreau viscosity function (2.2), the zero-shear-rate viscosity η_0 was taken equal to one, so that three dimensionless parameters were needed to defined the flow: Re, λ_c, and n.

Figure 6.6 shows a uniform criss-crossed Mesh C generated by Delauay triangular grids with 16 partitions per unit length. Recall that for the flow in a planar channel, it is necessary to choose proper weights K in the LS method to obtain accurate results. In the second example, using weights ranging from $K = 1$ to $K = 10^8$ in the LS functional on Mesh C, the values of the functional $g^{1/2}$ are shown in Table 6.2 for the Newtonian model at $Re = 1$ and 100, and for the Carreau model at $Re = 1$, $\lambda_c = 10$, and $n = 0.5$. The results indicate that when $K \ge 10^5$, we obtained convergence of the functional $g^{1/2}$. Therefore, setting $K = 10^5$ is sufficient to obtain satisfactory results. The mass conservation parameter $K = 10^5$ is chosen in the least-squares formulations in the second example.

In our computations, Mesh C is considered as the initial mesh. Refined mesh conver-

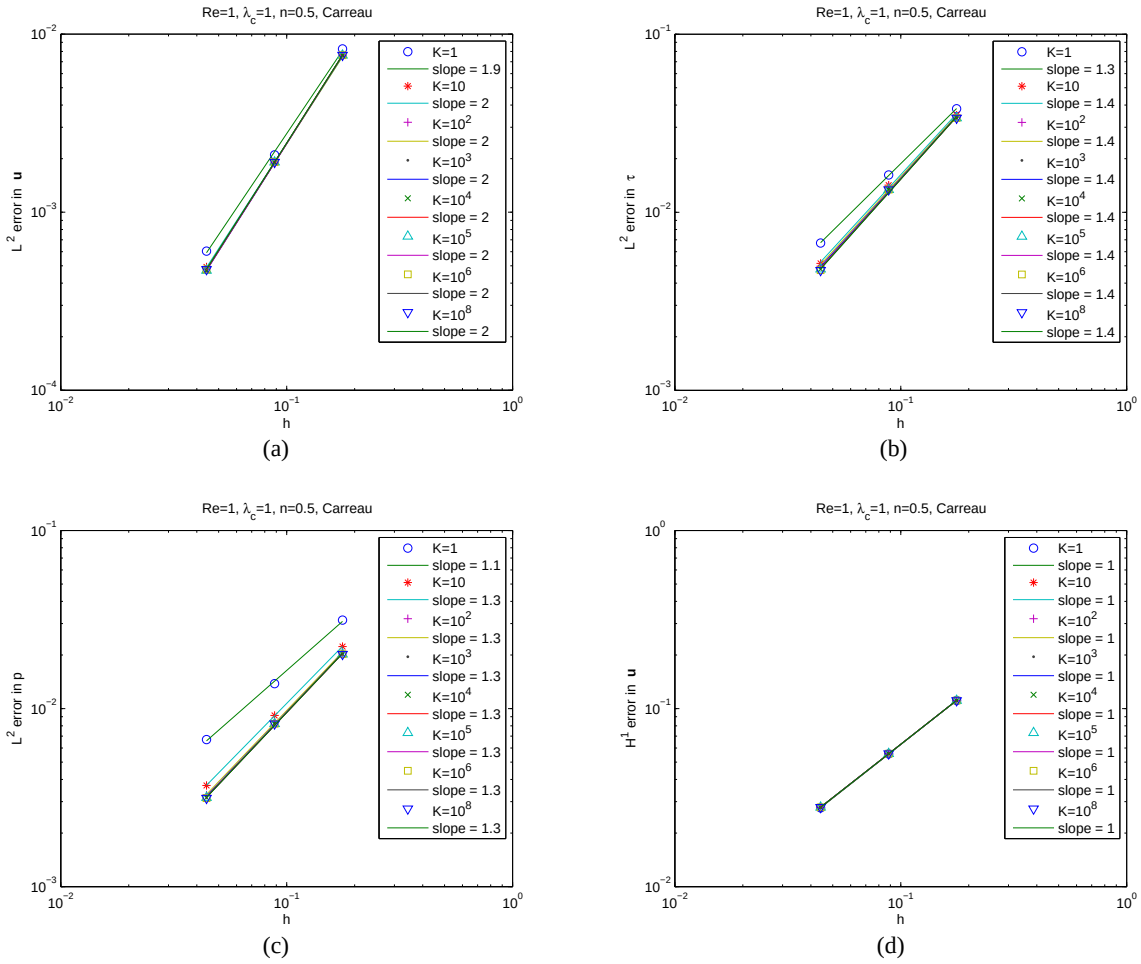

FIG. 6.3. *Errors in least-squares solutions with various weights K for Carreau model at* $Re = 1$, $\lambda_c = 1$, *and* $n = 0.5$. *L^2 errors in (a)* $\mathbf{u}$, *(b)* $\boldsymbol{\tau}$, *(c) p, and (d) H^1 errors in* $\mathbf{u}$.

	$Re = 1$, Newtonian		$Re = 100$, Newtonian		$Re = 1$, Carreau	
Weight K	Steps	$g^{1/2}$	Steps	$g^{1/2}$	Steps	$g^{1/2}$
1	2	0.00077	4	0.00077	3	0.000769
10^1	2	0.00074	4	0.000712	12	0.001322
10^2	3	0.010137	5	0.000439	5	0.007039
10^3	3	0.079862	8	0.0001	5	0.007658
10^4	3	0.119331	6	0.000022	5	0.007722
10^5	3	0.124843	6	0.000027	5	0.007728
10^6	3	0.125416	6	0.000028	5	0.007729
10^7	3	0.125474	6	0.000028	5	0.007729
10^8	3	0.125479	6	0.000028	5	0.007729

TABLE 6.2

Least-squares method on Mesh C for Newtonian model at $Re = 1$ *and* $Re = 100$ *and Carreau model at* $Re = 1$, $n = 0.5$, *and* $\lambda_c = 10$. *Nonlinear functional norm $g^{1/2}$ in nonlinear nested iteration for various weights K. Here steps means the number of Newton steps.*

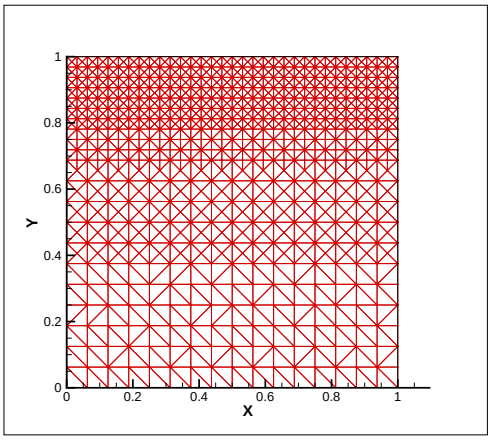

(a) Mesh DA

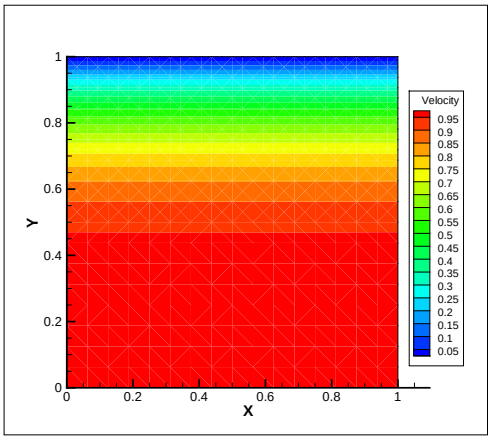

(b) Velocity contour on Mesh DA

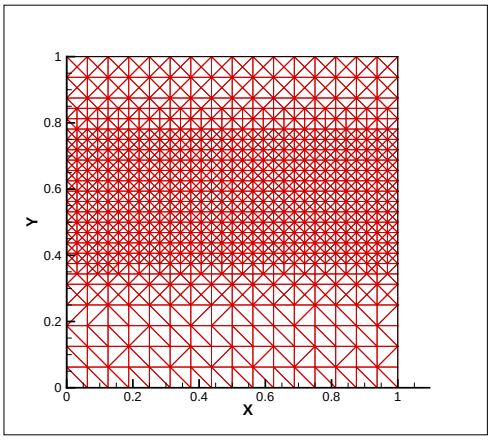

(c) Mesh DB

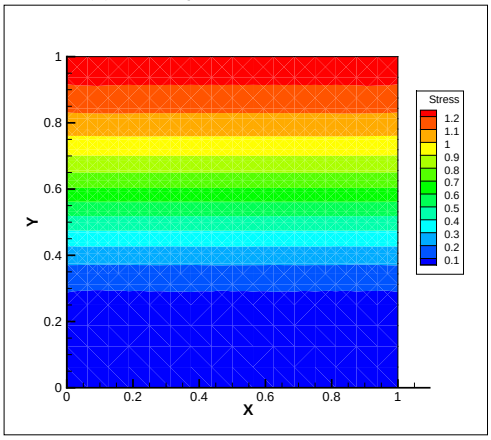

(d) Stress contour on Mesh DB

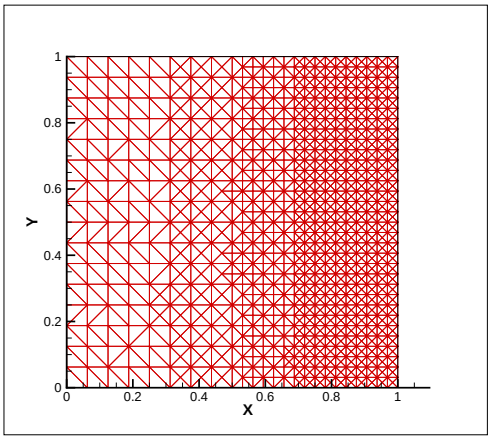

(e) Mesh DC

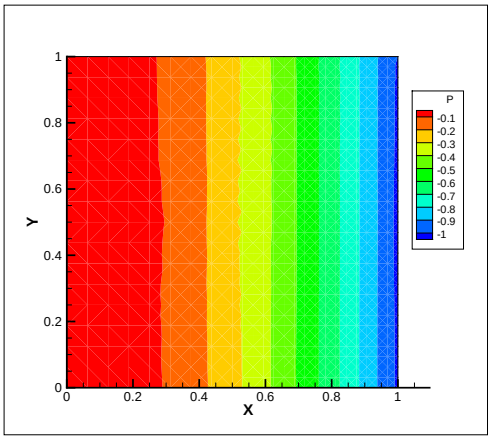

(f) Pressure contour on Mesh DC

FIG. 6.4. *Carreau model at* $Re = 1$, $\lambda_c = 1$, *and* $n = 0.5$. *Convergent adaptively refined Meshes DA, DB, and DC with two iterations respectively generated by velocity, stress, and pressure and their contours.*

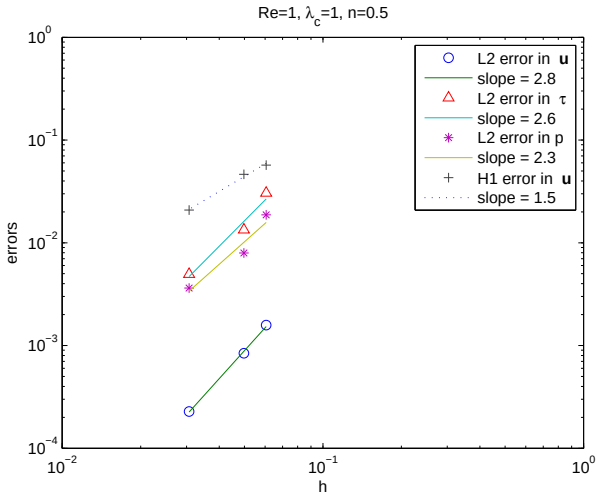

FIG. 6.5. *Errors in AR-LS solutions for Carreau model at* $Re = 1$, $\lambda_c = 1$, *and* $n = 0.5$.

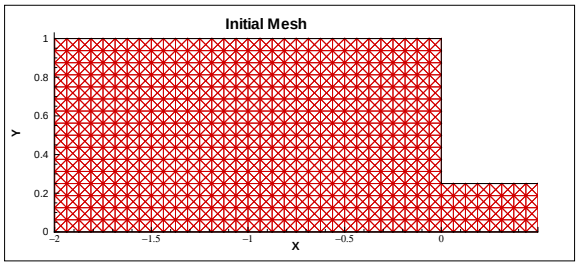

Mesh C

FIG. 6.6. *Mesh C is a uniform criss-crossed mesh with 16 partitions per unit length.*

gence was declared when the norm of the residual in minimum mesh length between two consecutive iterations was less than 0.005, which can be achieved within three iterations. Figures 6.7(a), (b), and (c) show three adaptive Meshes, CA1, CA2, and CA3, generated by the AR-LS method for the Newtonian model ($Re = 1$ and $Re = 100$) and the Carreau model ($Re = 1$, $\lambda_c = 10$, $n = 0.5$), respectively, using Mesh C as the initial mesh. The results show that these adaptive meshes are more refined near the reentrant corner and downstream boundary layers. Figures 6.8, 6.9, and 6.10 show contours of the vertical velocity v on Meshes C and CA1 for the Newtonian model at $Re = 1$, those on Meshes C and CA2 for the Newtonian model at $Re = 100$, and those on Meshes C and CA3 for the Carreau model at $Re = 1$, $\lambda_c = 10$, and $n = 0.5$, respectively. The results show that contours of the vertical velocity v on Mesh C are not smooth enough, and contours of v on the adaptively refined Meshes CA1, CA2, and CA3 provide a better contraction impression than does Mesh C, which reveals that the refinement results are of good quality. Figure 6.11 shows that the convergence rates in $g^{1/2}$ of the AR-LS solutions for the Newtonian model at $Re = 1$ and $Re = 100$, and for the Carreau model ($Re = 1$, $\lambda_c = 10$, $n = 0.5$) are 1.4, 1.3, and 1.6, respectively. The figure results reveal that the functional $g^{1/2}$ approaches the optimal convergence rates $O(h)$ for all cases. In Figure 6.12, we display a comparison between our AR-LS results and the GLS results of Zinani and Frey

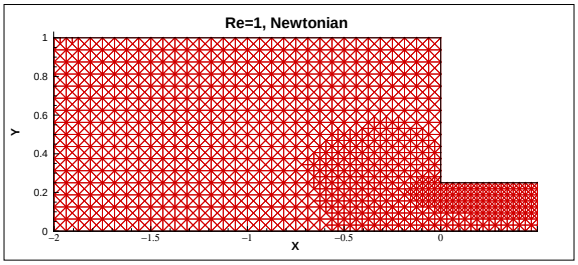

(a) Mesh CA1

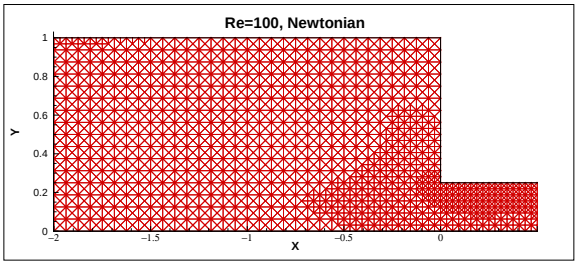

(b) Mesh CA2

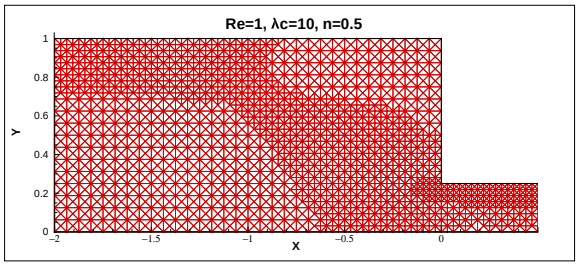

(a) Mesh CA3

FIG. 6.7. *Adaptively refined meshes with two iterations using the initial Mesh C for Newtonian model: (a) Mesh CA1 for* $Re = 1$*, (b) Mesh CA2 for* $Re = 100$*, and (c) Mesh CA3 for Carreau model at* $Re = 1$*,* $n = 0.5$*, and* $\lambda_c = 10$*.*

[3] for the horizontal velocity u profiles along the symmetric line in the contraction plane for the Newtonian model ($Re = 1$ and $Re = 100$) and the Carreau model ($Re = 1$, $\lambda_c = 10$, $n = 0.5$). We show the same for the profiles of $u(x,0)$ along the symmetric line by employing two adaptive meshes with minimum grid sizes h_{min} of 0.03125 and 0.015625. Accordingly, we obtained convergent velocity profiles by using the AR-LS method in all cases, as shown in Figure 6.12. The figure also shows that the profiles used in the AR-LS method are similar to those used in the GLS method by Zinani and Frey [3], except for the velocity profile near the contraction when the Reynolds number is high ($Re = 100$). The results show that the main differences likely occurred because of inertia effects, that is, the AR-LS method would be sensitive to high Reynolds numbers for resolving the singularities arising from geometric discontinuities. The issue will be investigated further in the future. Nevertheless, we obtain the same maximum velocity for all cases in the regions of the fully developed flow, as shown in [3]. It is assumed that the results are in good agreement.

We next evaluate the effects of power-law indices n and Carreau time number λ_c on adaptive meshes. For $\lambda_c = 1$ and $Re = 1$ in the Carreau model, we employed $n = 0.75$, 0.5, 0.25, and 0.125 in Figure 6.13. For $n = 0.5$ and $Re = 1$, we considered $\lambda_c = 0.1$ and 100 in Figure 6.14. Because of the shear thinning effect in the Carreau model, the results show that adaptively refined meshes depend on shear thinning physical behavior and are refined along the large variation area of the flow. For $Re = 1$ and $\lambda_c = 1$, the profiles of the horizontal velocity component u in the contraction plane along $x = 0$ with indices $n = 0.75$, 0.5, 0.25, and 0.125 in the Carreau viscosity function are presented in Figure 6.15(a). The figure results show that when $n = 0.125$, the shear thinning fluid velocity near the wall is higher than other values of n, causing the flattest velocity profile in the contraction plane. Because the low index fluid near the wall has low viscosity, the velocity growth rate away from the wall of the low power-law index fluid is greater than the high index fluid. To evaluate the effects

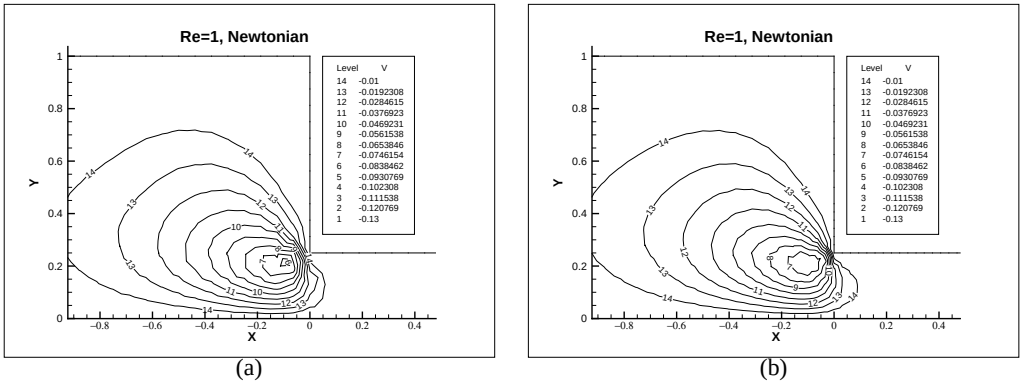

FIG. 6.8. *Contours of the vertical velocity v on (a) Mesh C and (b) Mesh CA1 for Newtonian model at* $Re = 1$.

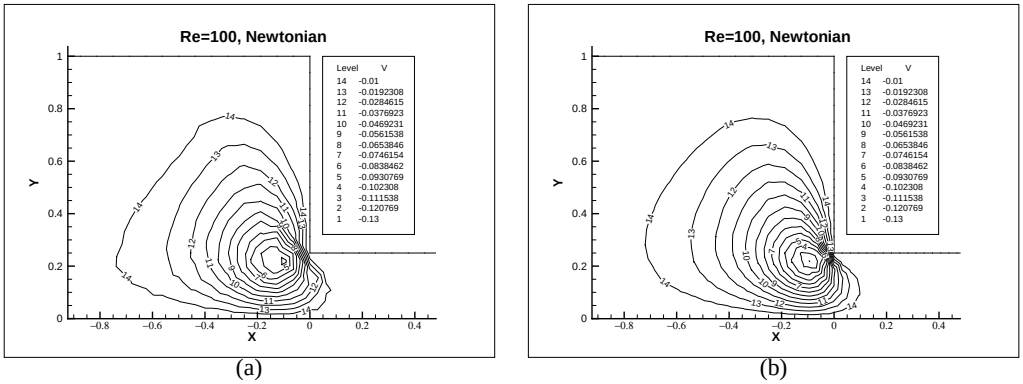

FIG. 6.9. *Contours of the vertical velocity v on (a) Mesh C and (b) Mesh CA2 for Newtonian model at* $Re = 100$.

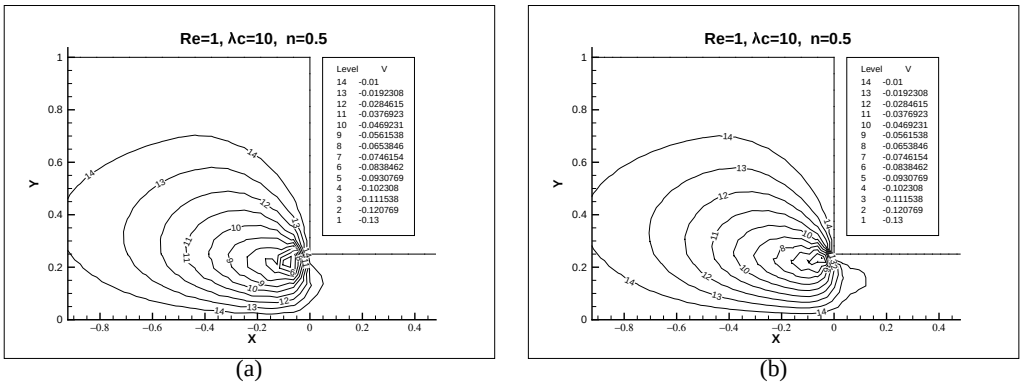

FIG. 6.10. *Contours of the vertical velocity v on (a) Mesh C and (b) Mesh CA3 for Carreau model at* $Re = 1$, $\lambda_c = 10$, $n = 0.5$.

of Carreau time number λ_c, we employed $\lambda_c = 0.1$, 1, 10, and 100 in the Carreau model at $n = 0.5$ and $Re = 1$ in Figure 6.15(b), which shows the horizontal velocity component u in the contraction plane along $x = 0$. The Carreau time number λ_c controls the fluid thinning effect

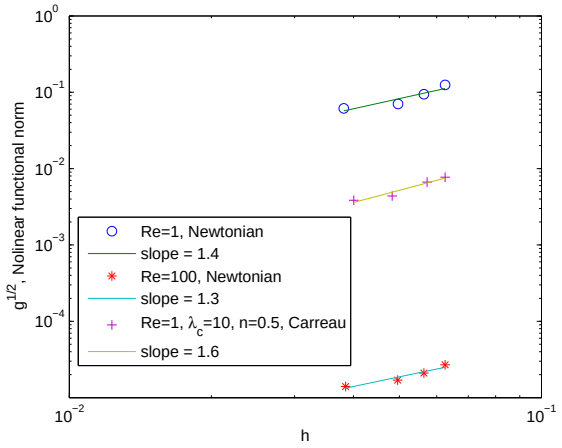

FIG. 6.11. *Nonlinear least-squares functional norm versus grid size h for Newtonian model at* $Re = 1$ *(o) and* $Re = 100$ *(*) and Carreau at* $Re = 1$, $\lambda_c = 10$, $n = 0.5$ *(+).*

and indicates the velocity growth rate away from the wall of the high λ_c fluid, which is greater than that of the low λ_c fluid. The figure also shows that the profiles used in the AR-LS method are similar to those used in the NWLS method by Chen et al. [4]. The results show that the effect of increasing λ_c is similar to that of decreasing n for a low flow, $Re = 1$, as expected. To evaluate the inertia effects, we employed $Re = 1$, 10, and 100 in the Carreau model at $n = 0.125$ and $\lambda_c = 0.1$ in Figure 6.16. In contrast to the case where $Re = 1$ and $Re = 10$, the velocity profile where $Re = 100$ reveals an obvious difference. The results indicate the inertia effect cannot be neglected in some cases of non-Newtonian fluid flows. We showed the effects of physical parameters on the velocity field agree with those obtained by Zinani and Frey [3].

Finally, we employed another least-squares finite element method to illustrate the capability of the adaptively refined algorithm. In [5], Bochev and Gunzburger introduced a weighted least-squares functional involving L^2-norms of the residuals of the momentum equation multiplied by a mesh dependent weight h and they applied it to the Stokes equations. They showed that with correctly chosen mesh-dependent weights, the approximations to the solutions of the Stokes equations are optimal. To evaluate the effects of mesh weight in the least-squares approach for solving the Navier−Stokes problem, we employed the following weighted least-squares functional J_ℓ^h for $\ell = 0,\ 1,\ 2,\ \ldots$ based on the adaptively refined algorithm (called the AR-WDLS method) for the Carreau model at $Re = 1$, $\lambda_c = 1$, and $n = 0.5$, as follows:

$$J_\ell^h(\mathbf{u}, p, \boldsymbol{\tau}; \mathbf{F}) = h^2 \left\| \mathbf{u}_\ell^h \cdot \nabla \mathbf{u} + \mathbf{u} \cdot \nabla \mathbf{u}_\ell^h - \nabla \cdot \boldsymbol{\tau} + \nabla p - \mathbf{f} \right\|_0^2 + \left\| \boldsymbol{\tau} - \frac{2}{Re}\mathbf{D}(\mathbf{u}) - \frac{2}{Re}\mathbf{D}(\mathbf{u}_\ell^h) G\left(\mathbf{u}_\ell^h, \mathbf{u}\right) - \mathbf{g} \right\|_0^2 + KRe^{-2} \|\nabla \cdot \mathbf{u}\|_0^2. \quad (6.8)$$

We obtained two convergent adaptively refined meshes generated by the AR-LS and AR-WDLS methods using $K = 10^5$ and their streamline patterns, as shown in Figure 6.17. Figure 6.17 shows that the two convergent adaptively refined meshes are different, and the sizes of the corner vortex, the distance between the vortex reattach point and the top corner, using the AR-LS and AR-WDLS methods were approximately 0.375 and 0.5625, respectively. The

results show that in comparison with the AR-LS solution, the recirculation zone of fluid in the AR-WDLS solution seems too large. Note that the AR-LS results agree with the NWLS results of Chen et al. [4]. Therefore, the AR-LS method outperforms the AR-WDLS method and yields results which are compatible to those presented in [4].

7. Conclusion. We presented an adaptively refined finite element approximation to the Carreau generalized Newtonian model. We provided an a prior error estimate for the linearized velocity-pressure-stress first-order system problem and showed numerical results supporting the estimate. To resolve the high gradient regions over the domain, we developed an adaptive mesh refinement based on the least-squares method. When we used continuous piecewise linear finite element spaces for all variables, properly adjusting the importance of the mass conservation and with adaptive mesh refinements, we obtained optimal convergence rates for all variables which are better than those of the theoretical prediction. The adaptively refined algorithm is efficient because we show the least-squares functional optimal convergence rate, and these adaptive meshes are refined along the large variation area of the flow, which agrees well with the physical attributes of the models. Adaptive refinement for the 4-to-1 contraction problem depends on the shear thinning physical behavior, and our results agree with those obtained in published GLS and NWLS results. Our results show that the adaptively refined meshes are automatic local grid refinement with different flow parameters, and the refinement results are of good quality. Finally, numerical experiments indicate that the AR-LS method can be extended to more general 4-to-1 contraction problems without major difficulty.

Acknowledgment. The research was supported by the National Science Council of Taiwan under contract number 100-2115-M-160-001 and Wenzao Ursuline University of Languages. The author thanks the reviewers for helpful comments which improved this paper.

REFERENCES

[1] Z. Chai, B. Shi, Z. Guo, F. Rong, Multiple-relaxation-time lattice Boltzmann model for generalized Newtonian fluid flows, J. Non-Newtonian Fluid Mech., 166 (2011), pp. 332-342.
[2] P. Neofytou, A 3rd order upwind finite volume method for generalised Newtonian fluid flows, Advances in Engineering Software, 36 (2005), pp. 664-680.
[3] F. Zinani, S. Frey, Galerkin least-squares multifield approximations for flows of inelastic non-Newtonian fluids, J. of Fluids Engineering, 130 (2008), pp. 1-14.
[4] T. F. Chen, C. L. Cox, H. C. Lee, K. L. Tung, Least-squares finite element methods for generalized Newtonian and viscoelastic flows, Appl. Numer. Math., 60 (2010), pp. 1024-1040.
[5] P. B. Bochev, M. D. Gunzburger, Finite element methods of least-squares type, SIAM, Revi., 40 (1998), pp. 789-837.
[6] S. Y. Yang, J. L. Liu, Least-squares finite element methods for the elasticity problem, J. Comput. Appl. Math., 87 (1997), pp. 39-60.
[7] P. B. Bochev, Analysis of least-squares finite element methods for the Stokes equations, Math. Comp., 63 (1994), pp. 479-506.
[8] P. B. Bochev, Analysis of least-squares finite element methods for the Navier−Stokes equations, SIAM J. Numer. Anal., 34 (1997), pp. 1817–1844.
[9] P. B. Bochev, Z. Cai, T. A. Manteuffel, S. F. McCormick, Analysis of velocity-flux first-order system least-squares principles for the Navier−Stokes equations:, Part I, SIAM J. Numer. Anal., 35 (1998), pp. 990–1009.
[10] P. B. Bochev, Z. Cai, T. A. Manteuffel, S. F. McCormick, Analysis of velocity-flux first-order system least-squares principles for the Navier−Stokes equations:, Part II, SIAM J. Numer. Anal., 36 (1998), pp. 1125-1144.
[11] P. Bolton, R. W. Thatcher, A least-squares finite element method for the Navier−Stokes equations, J. Comput. Phys., 213 (2006), pp. 174-183.
[12] J. J. Heys, E Lee, T. A. Manteuffel, S. F. McCormick, An alternative least-squares formulation of the Navier−Stokes equations with improved mass conservation, J. of Comput. Phys., 226 (2007), pp. 994-1006.

[13] J. M. Deang, M. Gunzburger, Issues Related to least-squares finite element methods for the Stoke equations, SIAM J. Sci. Comput. 20 (1998), pp. 878-906.
[14] A. Bose, G. F. Carey, Least-squares p-r finite element methods for incompressible non-Newtonian flows, Comput. Methods Appl. Mech. Engrg., 180 (1999), pp. 431-458.
[15] H. C. Lee, T. F. Chen, A nonlinear weighted least-squares finite elements method for Stokes equations, Comput. Math. Appl., 59 (2010), pp. 215-224.
[16] H. C. Lee, A nonlinear weighted least-squares finite element method for the Oldroyd-B viscoelastic flow, Appl. Math. Comput., 219 (2012), pp. 421-434.
[17] J. Azaiez, R. Guénette, A. Ait-Kadi, Numer. simulation of viscoelastic flows through a planar contraction, J. Non-Newtonian Fluid Mech., 62 (1996), pp. 253-277.
[18] M. J. Berger, A. Jameson, Automatic adaptive grid refinement for the Euler equations, AIAA, J., 23 (1985), pp. 561-568.
[19] H. De Sterck, T. Manteuffel, S McCormick, J Nolting, J. Ruge, L. Tang, Efficiency-based h- and hp-refinement strategies for finite element methods, Numer. Linear Algebra with Appl., 15 (2008), pp. 89-114.
[20] Z. Cai, C. R. Westphal, An adaptive mixed least-squares finite element method for viscoelastic fluids of Oldroyd type, J. Non-Newtonian Fluid Mech., 159 (2009), pp.72-80.
[21] J. H. Adler, T. A. Manteuffel, S. F. McCormick, J. W. Nolting, J. W. Ruge, L. Tang, Efficiency based adaptive local refinement for first-order system least-squares formulations, SIAM J. Sci. Comput., 33 (2011), pp. 1-24.
[22] H. C. Lee, Adaptive least-squares finite elements methods for viscoelastic flow problems, Ph.D. thesis, Dept. of Math., National Chung Cheng University, Taiwan, 2008.
[23] S. D. Kim, B.C. Shin, H^{-1} least-squares method for the velocity-pressure-stress formulation of Stokes equation, Appl. Numer. Math., 40 (2002), pp. 451-465.
[24] T. F. Chen, H. Lee, C. C. Liu, Numer. approximation of the Oldroyd-B model by the weighted least-squares/discontinuous Galerkin method, Numer. Methods for Partial Differential Equations, 29 (2013), pp. 531-548.
[25] S. S. Shibeshi, W. E. Collins, The rheology of blood flow in a branched arterial system, Appl Rheol., (2005), 15(6), pp. 398-405.
[26] N. Ali, T. Hayat, Peristaltic motion of a Carreau fluid in an asymmetric channel, Appl. Math. Comput., 193 (2007), pp. 535-552.
[27] H. C. Lee, T. F. Chen, A nonlinear weighted least-squares finite elements method for the velocity-vorticity-pressure formulation of the Stokes equations, Appl. Math. Comput., submitted.
[28] C. C. Tsai, S. Y. Yang, On the velocity-vorticity-pressure least-squares finite element method for the stationary incompressible Oseen problen, J. Comp. Appl. Math., 182 (2005), pp. 211-232.
[29] J. R. Shewchuk, Triangle: Engineering a 2D quality mesh generator and Delaunay triangulator, in "Appl. Computational Geometry: Towards Geometric Engineering", Lecture Notes in Comput. Sci., 1148, Springer, New York, 1996, pp. 203-222.
[30] C. Băcuţă, V. Nistor, L. Zikatanov, Improving the rate of convergence of 'high order finite elements' on polygons and domains with cusps, Numer. Math., 100 (2005), pp. 165-184.
[31] Z. Cai, T. A. Manteuffel, S. F. McCormick, First-order system least squares for second-order partial differential equations. II, SIAM J. Numer. Anal. 34 (1997), pp. 425-454 .

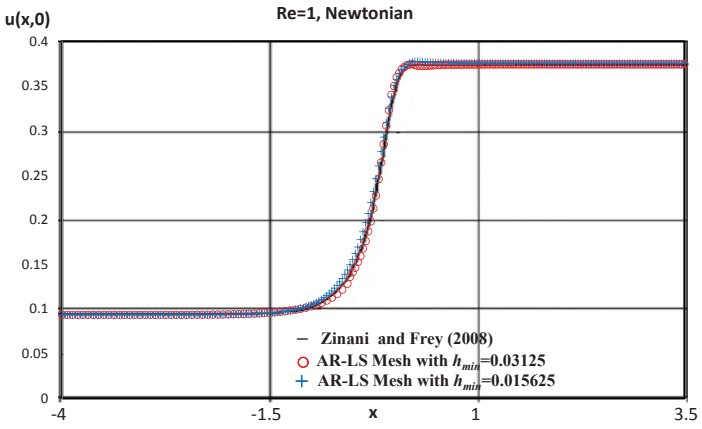

(a)

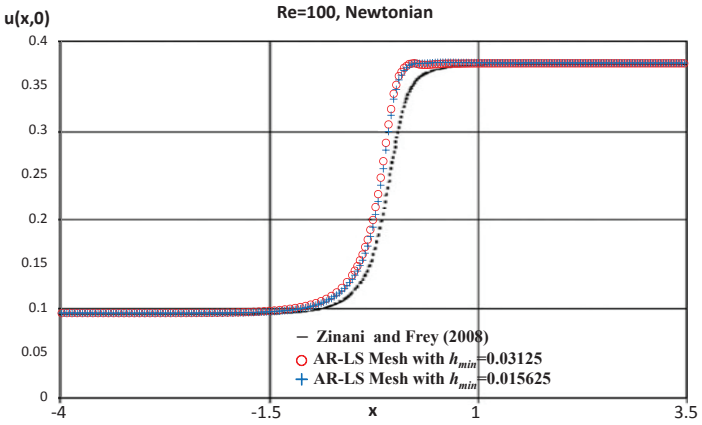

(b)

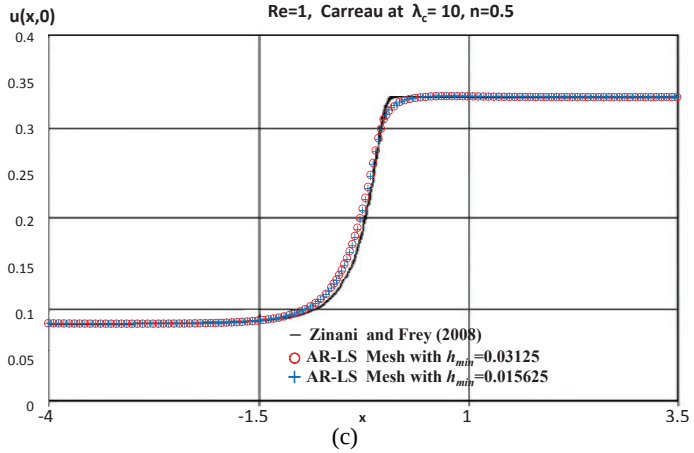

(c)

FIG. 6.12. *Profiles of the horizontal velocity $u(x,0)$ along the symmetric line for (a) Newtonian model at $Re = 1$, (b) Newtonian model at $Re = 100$, and (c) Carreau model at $Re = 1$, $\lambda_c = 10$, and $n = 0.5$.*

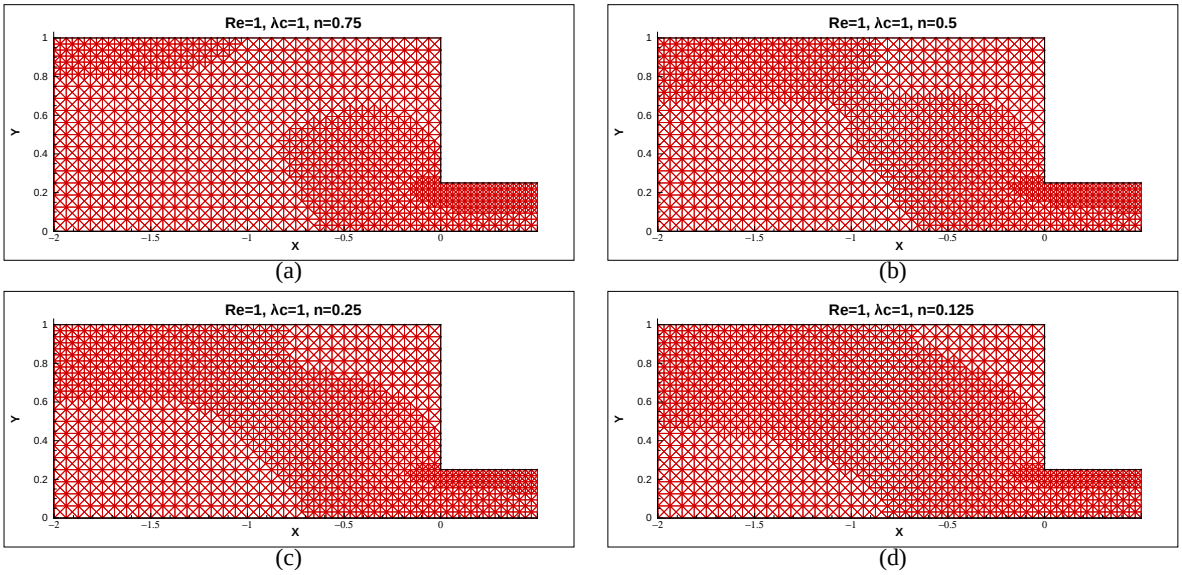

(a) (b) (c) (d)

FIG. 6.13. *Carreau model at* $Re = 1$, $\lambda_c = 1$. *Adaptive refined meshes at (a)* $n = 0.75$, *(b)* $n = 0.5$, *(c)* $n = 0.25$, *and (d)* $n = 0.125$.

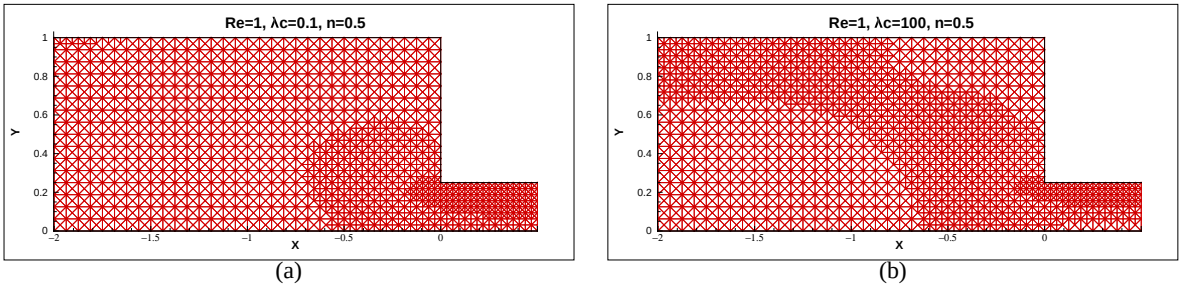

(a) (b)

FIG. 6.14. *Carreau model at* $Re = 1$, $n = 0.5$. *Adaptive refined meshes at (a)* $\lambda_c = 0.1$ *and (b)* $\lambda_c = 100$.

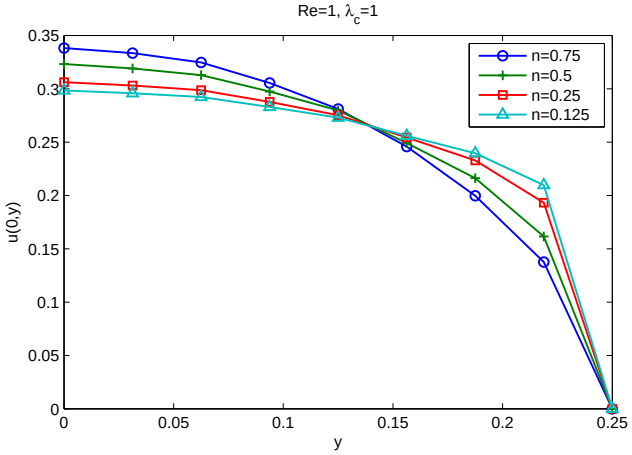

(a)

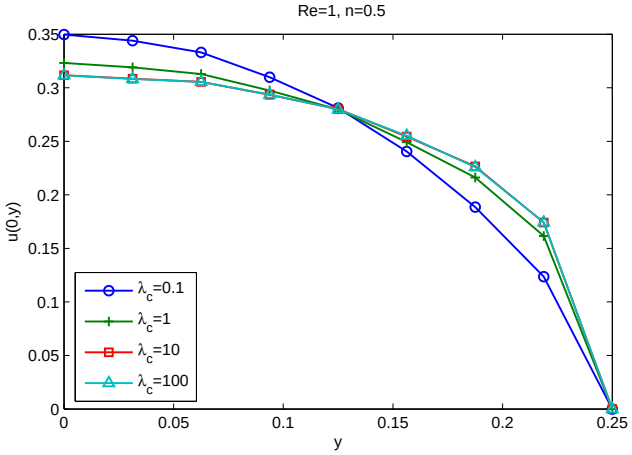

(b)

FIG. 6.15. *Profiles of the horizontal velocity* $u(0,y)$ *at (a)* $Re = 1$, $\lambda_c = 1$ *for* $n = 0.75$ *(o),* $n = 0.5$ *(+),* $n = 0.25$ *(□),* $n = 0.125$ *(△), and (b)* $Re = 1$, $n = 0.5$ *for* $\lambda_c = 0.1$ *(o),* $\lambda_c = 1$ *(+),* $\lambda_c = 10$ *(□),* $\lambda_c = 100$ *(△).*

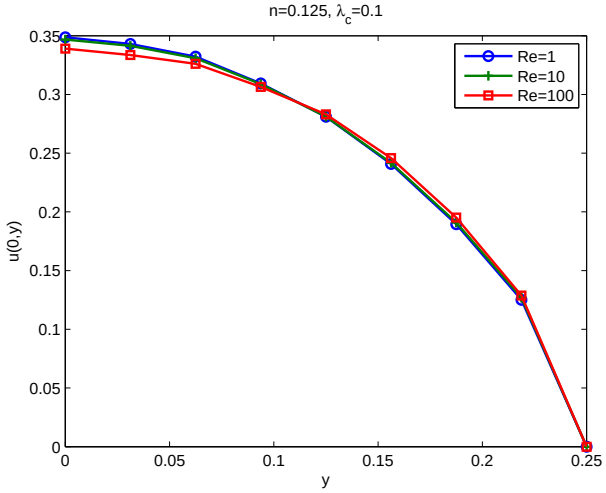

FIG. 6.16. *Profiles of the horizontal velocity* $u(0,y)$ *at* $n = 0.125$, $\lambda_c = 0.1$ *for* $Re = 1$ *(o),* $Re = 10$ *(+), and* $Re = 100$ *(□).*

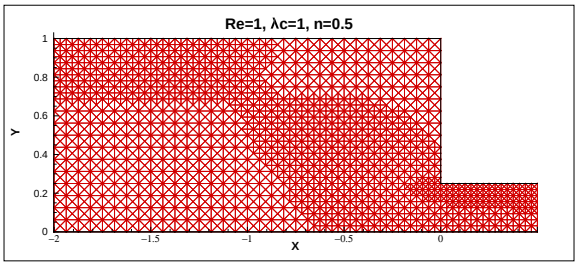

(a) AR-LS mesh

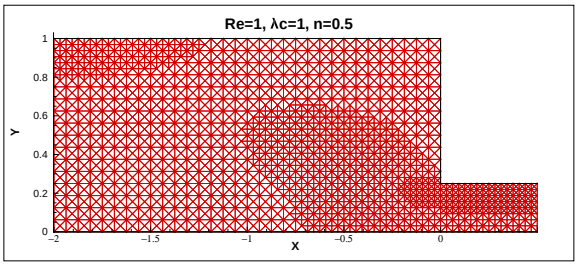

(b) AR-WDLS mesh

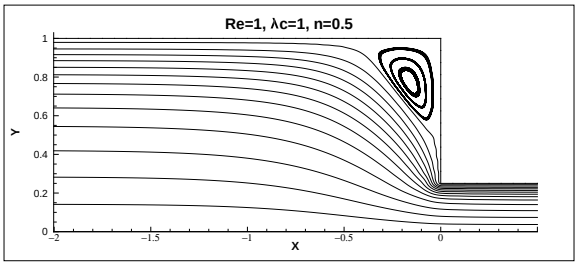

(c) Streamlines in AR-LS

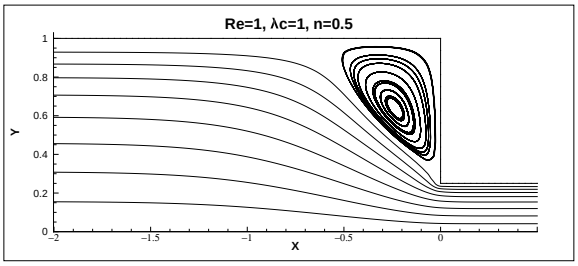

(d) Streamlines in AR-WDLS

FIG. 6.17. *Carreau model at* $Re = 1$, $\lambda_c = 1$, *and* $n = 0.5$. *Adaptive refined meshes of the (a) AR-LS and (b) AR-WDLS methods. Streamlines in (c) AR-LS and (d) AR-WDLS solutions.*